A tale of two phase diagrams: Interplay of ordering and hydrogen uptake in Pd–Au–H

Citation for the original published paper (version of record):

Rahm, M., Löfgren, J., Fransson, E. et al (2021). A tale of two phase diagrams: Interplay of ordering and hydrogen uptake in Pd–Au–H. Acta Materialia, 211.
http://dx.doi.org/10.1016/j.actamat.2021.116893

Acta Materialia 211 (2021) 116893

Contents lists available at ScienceDirect

Acta Materialia

journal homepage: www.elsevier.com/locate/actamat

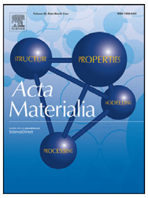

A tale of two phase diagrams: Interplay of ordering and hydrogen uptake in Pd–Au–H

J. Magnus Rahm, Joakim Löfgren, Erik Fransson, Paul Erhart*

Chalmers University of Technology, Department of Physics, S-412 96 Gothenburg, Sweden

ARTICLE INFO

Article history:
Received 12 February 2021
Revised 8 April 2021
Accepted 10 April 2021
Available online 17 April 2021

ABSTRACT

Due to their ability to reversibly absorb/desorb hydrogen without hysteresis, Pd–Au nanoalloys have been proposed as materials for hydrogen sensing. For sensing, it is important that absorption/desorption isotherms are reproducible and stable over time. A few studies have pointed to the influence of short and long range chemical order on these isotherms, but many aspects of the impact of chemical order have remained unexplored. Here, we use alloy cluster expansions to describe the thermodynamics of hydrogen in Pd–Au in a wide concentration range. We investigate how different chemical orderings, corresponding to annealing at different temperatures as well as different external pressures of hydrogen, impact the behavior of the material with focus on its hydrogen absorption/desorption isotherms. In particular, we find that a long-range ordered $L1_2$ phase is expected to form if the H_2 pressure is sufficiently high. Furthermore, we construct the phase diagram at temperatures from 250 K to 500 K, showing that if full equilibrium is reached in the presence of hydrogen, phase separation can often be expected to occur, in stark contrast to the phase diagram in para-equilibrium. Our results explain the experimental observation that absorption/desorption isotherms in Pd–Au are often stable over time, but also reveal pitfalls for when this may not be the case.

1. Introduction

The prospect of hydrogen as a replacement for fossil fuels continues to generate interest in metallic hydrides. Some metals are of particular interest in this context as they can be reversibly loaded and unloaded with hydrogen by tuning the partial pressure of H_2 gas in the environment; Pd is one such example. When loaded with hydrogen, the Pd hydride has a hydrogen density that is orders of magnitudes larger than H_2 gas under the same conditions, and it is therefore a candidate for storing hydrogen [1]. Another potential application of Pd hydrides is sensing [2,3]. Pd nanoparticles that are exposed to hydrogen quickly form a hydride [4], and when doing so, their optical properties change. This change can be easily detected, and Pd nanoparticles can thus be used as reversible hydrogen sensors [5,6]. The use of Pd for hydrogen sensing applications has, however, a major disadvantage; Pd hydride formation at room temperature is associated with a first-order phase transition from a hydrogen-poor α phase to a hydrogen-rich β phase, which causes the sensor response to be a highly non-linear function of H_2 pressure. Since the phase transition is also associated with hysteresis [7–9], the response moreover differs between the loading and unloading half-cycles. These aspects are generally unfavorable for sensing applications.

Fortunately, these drawbacks can be alleviated by alloying Pd with Au. With around 20 mol-% of Au in Pd, the system can be loaded continuously with hydrogen [10,11], eventually making the sensor readout an almost linear function of H_2 pressure [12–15]. The introduction of another chemical species thus fundamentally changes the thermodynamics of the material and improves its properties. From a scientific as well as practical standpoint, however, an alloy is significantly more complex than a pure metal, and multiple important questions arise: what is the optimal composition, how are the chemical elements ordered under different circumstances, and how does this ordering influence the properties of the material? The influence of overall composition can usually be relatively easily optimized by experimental screening. The chemical ordering, on the other hand, is difficult to both control and measure experimentally, and can be expected to be influenced by conditions during and after fabrication. Moreover, although Pd–Au nanoalloy sensors tend to be stable over time [16], changes may occur over long time-scales due to slow kinetics, which makes the effects tedious to experimentally assess, while they may still be detrimental to the material. Although the study of hydrogen in

---

* Corresponding author.
E-mail address: erhart@chalmers.se (P. Erhart).

https://doi.org/10.1016/j.actamat.2021.116893

Pd and its alloys has a long and rich history [7,17–23], many fundamental aspects of the Pd–Au–H system are still unknown, and to fully exploit this material it is of paramount importance that its thermodynamics are understood, as it determines the driving forces that underpin the evolution of the atomic scale structure over time.

A few previous studies have successfully used combinations of density-functional theory (DFT) calculations and statistical methods to predict properties of hydrogen in Pd–Au. For example, Mamatkulov and Zhdanov [24] recently developed a model based on DFT calculations that successfully predicted absorption isotherms, highlighting that once octahedral sites without surrounding Au atoms become few, the phase transition and its associated hysteresis disappears. These calculations assumed a Pd–Au lattice with random configuration, which remained unaffected by insertion of hydrogen. This metastable equilibrium, with equilibrium only on the hydrogen sublattice, is commonly referred to as para-equilibrium [25–27]. If the metal atoms are allowed to rearrange in response to hydrogen such that full equilibrium is reached, a significantly more complex phase diagram can be expected [28]. This was indicated experimentally by Lee *et al.* [29], who found that long-range order (LRO) was formed in Pd–Au with 19% Au when subjected to a high pressure of H_2 at high temperatures. Importantly, alloys with this LRO had strikingly different pressure–composition isotherms than those that had not been treated in a high-pressure H_2 gas and lacked LRO. A similar conclusion was reached by Chandrasekhar and Sholl *et al.* [30], who computed hydrogen solubility as a function of chemical order at Au contents 4% and 15%. These results show that the different degrees of equilibration matter for the properties of the Pd–Au–H system, and since many applications depend on reproducible pressure–composition isotherms, chemical order should not be ignored. In this light, it is obvious that a full accounting of the impact of chemical order on the thermodynamics of Pd–Au–H is desirable.

Here, we make a detailed atomic scale study of the thermodynamics of hydrogen in Pd–Au. To this end, we use alloy cluster expansion fitted to DFT to describe the energetics of the system ranging from 0% to 50% Au in Pd and in the full range from no hydrogen to full hydrogen occupation. This approach, which has been successfully applied to similar materials in the past [30–34], allows for very fast evaluation of the energy of a system with hundreds of atoms with an accuracy approaching that of DFT. Using Monte Carlo (MC) simulations, we can elucidate the thermodynamics and, in particular, study how chemical order evolves under different circumstances.

2. Methodology

Our methodology comprises the following steps: (1) we calculate energies of Pd–Au–H structures with different composition and configuration [35,36] with DFT [37–40], (2) fit alloy cluster expansion to these energies [41], and (3) sample the system using MC simulations in different ensembles using the ICET software [36]. The details of these methods are provided in Supplementary Note 1–3. With this methodology, we can extract temperature-dependent thermodynamic quantities with a high accuracy.

In Pd–Au–H, hydrogen primarily occupies octahedral interstitial sites in the face-centered cubic (FCC) lattice formed by Pd–Au (although in some configurations, tetrahedral site may be preferred [24,42]). The full system can thus be viewed as a rock salt structure, i.e., two interpenetrating FCC sublattices, one occupied by Pd and Au, and the other populated with H and vacancies. In the following, we will state concentrations *per sublattice*, such that, for example, the H concentration is 100% if all sites on the H/vacancy sublattice are occupied by H, whereas energies are stated per formula unit (f.u.) with a f.u. being two sites, one per sublattice. We restricted our training data (and simulations) to Au concentration below 50%, and excluded training data with too large relaxation relative to the reference lattice (as detailed in Supplementary Note 2).

To be able to quantify the uncertainty stemming from the fitting of the cluster expansion (CE) model, we used a Bayesian approach to construct 10 additional CE models [43,44], below referred to as “sampled cluster expansion”. The results below were, however, obtained with the average CE model unless stated otherwise.

In this work, we exploit the possibility to sample the two sublattices with different strategies in the same MC simulation. Specifically, we used different combinations of the canonical, semi-grand canonical (SGC), and variance-constrained semi-grand canonical (VCSGC) [45,46] ensembles. MC simulations in the canonical ensemble involve swapping the chemical identity of two randomly chosen sites on the same sublattice, whereas SGC and VCSGC simulations only involve flipping the chemical identity of one site at a time. The overall composition is thus preserved in the canonical ensemble but not in the SGC or VCSGC ensemble. The canonical ensembles is thus closely related to closed systems (which is usually the case for the Pd–Au sublattice experimentally), whereas the SGC and VCSGC ensemble mimic open systems (which is almost always the case for the H–vacancy sublattice). The SGC and VCSGC ensembles also yield access to the free energy derivative $\partial F/\partial c$, and by extension the partial pressure of H_2, as discussed in Supplementary Note 4. By integration, the free energy landscape can be mapped out and phase diagrams constructed, as detailed in Supplementary Note 6.

3. Results and discussion

3.1. Cluster expansion construction

The CE constructed in this work has a root mean square error for the mixing energies of 8.3meV/f.u. over the training set and of 15.3meV/f.u. over the test set. To put these number in perspective, it is instructive to compare them to the wide span (−100 to 500meV/f.u.) of mixing energies in this system (Fig. 1). The largest errors are frequently found among structures with a large content of Au, which partially explains the large difference in error between training and test set, as the latter contained a higher proportion of structures with high Au content. The predicted energy of all structures (including structures that relaxed too far relative to the reference structure (see Fig. S2) but excluding those with $c_{\mathrm{Au}} > 0.5$) has a good albeit not perfect correlation with the corresponding DFT energies (Fig. 1a, $R^2 = 0.934$). The energies of structures with long relaxation distances are sometimes severely overestimated. This is unsurprising since they were not included in the training data and cannot be expected to be well described by the CE in any case. Many of the poorly described structures are those with higher mixing energies in a series of configurations with the same composition (Fig. 1b–g), and hence are in general less relevant for the thermodynamics of the system.

The effective cluster interactions (ECIs) of the constructed CE exhibit physically sound behavior in the sense that the strongest interactions are those that occur at a short distance, and triplet interactions are generally smaller than pair interactions (Fig. 2). Based on the ECIs, we can already at this point anticipate roughly how the system will behave. The strongest interaction is the one between Au/Pd and its nearest neighbor H/vacancy. We can anticipate that H will be attracted to Pd and vacancies to Au. H–H interactions, on the other hand, are comparatively weak, whereas the positive, short-ranged Au/Pd–Au/Pd ECI indicate that the formation of Pd–Au pairs is energetically favorable.

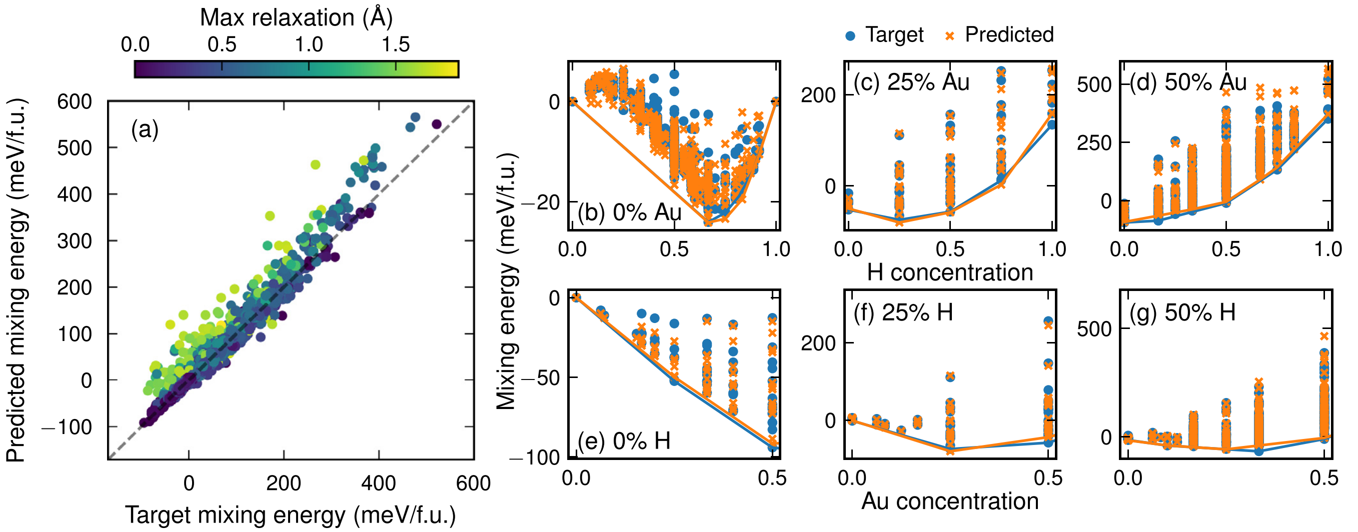

Fig. 1. Mixing energies as predicted with the CE developed in this work compared to target energies from DFT calculations. Structures for which the largest relaxation distance was small (dark blue dots in (a)) are generally well reproduced by the CE, whereas the energy of structures with large relaxation distances are overestimated by the CE (yellow dots in (a)). Only structures with maximum relaxation distance less than 0.5Å were included when training the CE. Mixing energies as a function of H concentration at fixed Au concentration (b–d) and as a function of Au concentration at fixed H concentration (e–g) reveal that the general energy landscape is well reproduced in the concentration intervals considered here.

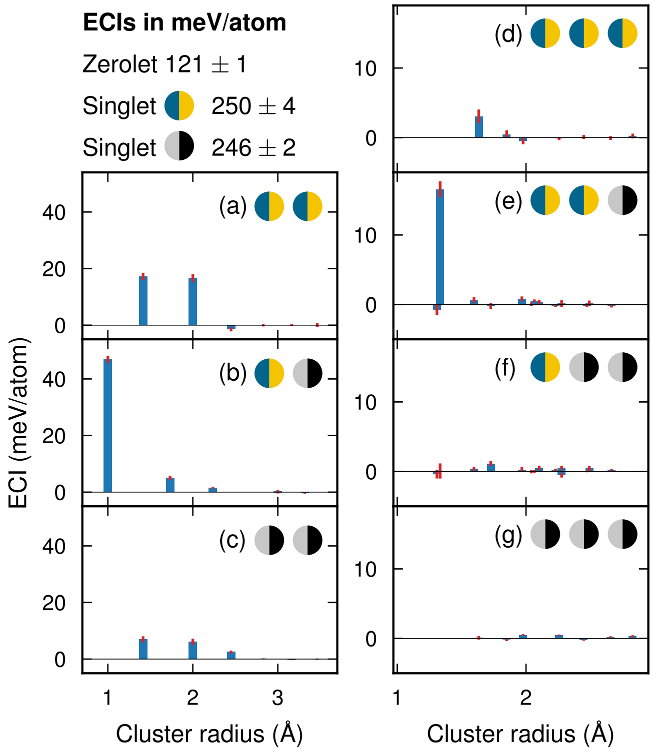

Fig. 2. Effective cluster interactions (ECIs) in the cluster expansion developed in this study, as function of the radius of the cluster, here defined as the average distance between the atoms in the cluster and their center of mass (assuming all atoms have the same mass). Pair ECIs are split in three categories, interactions between Au/Pd and Au/Pd (a), between Au/Pd and H/vacancy (b), and between H/vacancy and H/vacancy (c). In the same vein, triplet interactions are split into four categories depending on the sublattices involved (d)–(g). Error bars, defined as two standard deviations over a set of 100 randomly sampled cluster expansions, are shown in red at the tip of each bar.

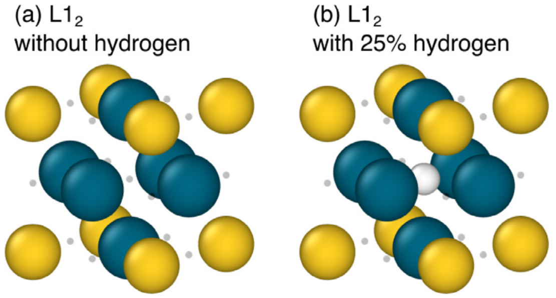

Fig. 3. The $L1_2$ phase without hydrogen (a) and with 25% hydrogen (b). Palladium, gold, and hydrogen are shown in blue, yellow, and white, respectively, whereas vacancies are shown as grey dots. In this ordered phase, hydrogen preferentially occupies the site surrounded by nearest neighbor Pd atoms. Note that this choice of cell does not give an accurate representation of compositions; the structures have (a) 25% Au and 75% Pd and (b) the same composition on the Pd–Au sublattice and 25% hydrogen and 75% vacancies on the other.

3.2. Ordered phases in hydrogen-free Pd–Au

Although the focus of our work is on the thermodynamics of hydrogen in Pd–Au, we begin our analysis with the Pd–Au alloy in absence of hydrogen as ordering on this sublattice turns out to be also relevant with regard to the hydrogenated system, as discussed below. As our CE is only fitted to structures with 50% Au or less, we restrict our analysis to this composition interval. The mixing energies of structures with 12 Pd/Au atoms or less are negative, meaning mixing is favorable (Fig. 1e). It is, however, still possible that phase separation occurs between ordered (intermetallic) phases. LRO in Pd–Au has been reported in experiments on thin films [47,48] and nanoparticles [49], but has generally not been found in the bulk, suggesting that the energetics causing ordering is either enhanced by surface stress or has critical temperatures too low for ordering to occur readily in bulk samples. By enumerating structures with up to 12 atoms in the cell, our CE identifies three structures on the convex hull between 0 and 50% Au: the trivial case of pure Pd, $AuPd_3$ in the $L1_2$ configuration (Fig. 3a) and AuPd in the $L1_0$ configuration. These findings are largely consistent with other computational studies, although other structures have occasionally been found on the convex hull [50,51].

To investigate at below which temperature the $L1_2$ phase will appear, we ran MC simulations in the canonical ensemble, i.e., with the composition fixed at 25% Au in Pd, and tracked the LRO parameter (see Supplementary Note 5) as a function of temperature. The

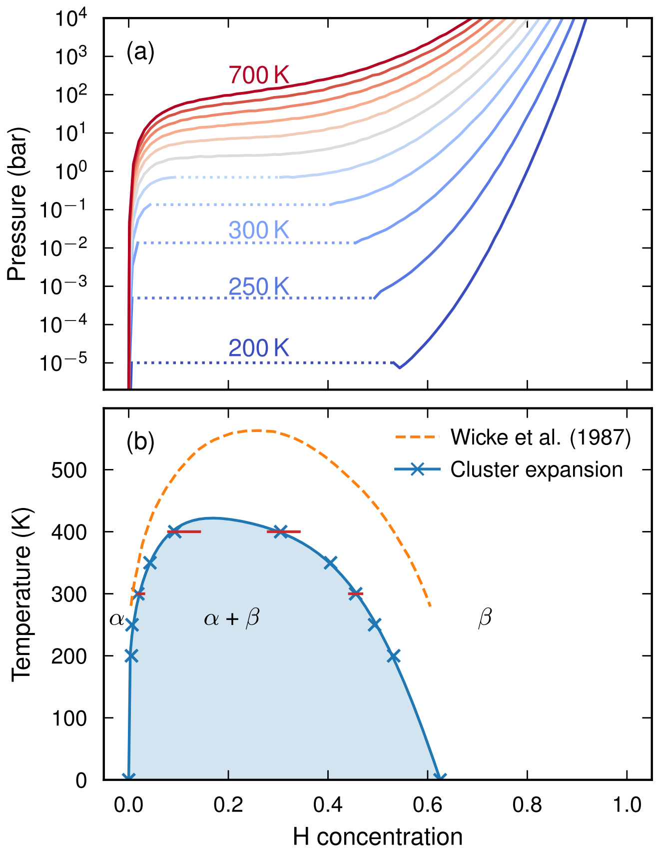

Fig. 4. Pressure–composition isotherms in steps of 50 K for pure Pd hydrides (a). Phase transitions from the hydrogen-poor α phase to the hydrogen-rich β phase have been drawn with a dashed line. These dashed lines indicate the phase boundaries of the two-phase region (blue crosses in (b), blue line is a fit to guide the eye). Compared to experimental results [52] (orange line in b), the critical temperature is underestimated, but the uncertainty from the choice of CE is significant, as indicated by the spread of the miscibility gap at 300 and 400 K from ten sampled CEs (red lines indicate difference between minimum and maximum value predicted by these ten CEs). Here, we have disregarded ordered phases with hydrogen concentrations above 0.67, all of which have critical temperatures below 200 K.

results revealed a critical temperatures at 180 K (Fig. S6), with a span among the sampled cluster expansion from less than 150 K to 260 K.

3.3. Hydrogen in pure Pd

We are now ready to add hydrogen to the system. Since the pure Pd hydride (no Au) has been more thoroughly studied than the alloy hydride, we begin in this limit. We carried out VCSGC-MC simulations on the H/vacancy lattice with temperatures between 200 K and 700 K in steps of 50 K. The thus obtained isotherms (Fig. 4a) indicate a low solubility of H in Pd until a “threshold pressure” has been reached. For sufficiently low temperatures, there is then a phase transition from a hydrogen-poor α phase to a hydrogen-rich β phase, which can be detected by integrating the free energy derivative and identify the regions where the free energy curve lies above its convex hull (as outlined in Supplementary Note 6). The corresponding phase diagram is largely consistent with the experimental phase diagram constructed by Wicke and Blaurock [52] (Fig. 4b). The critical temperature, which is challenging to estimate accurately both experimentally and by means of MC simulations, differs approximately 140 K (560 K experimentally and 420 K based on our CE). Although this is a fairly large discrepancy, it should be noted that small variations in the ECIs have a large impact on the critical temperature; at temperatures close to the critical temperature, uncertainties in the phase boundary become large (quantified by ten sampled cluster expansion; the spread from these ten cluster expansion is indicated with red horizontal bars in Fig. 4b). Discrepancies between simulation and experiment are thus not unexpected, especially given that it is also challenging to construct the phase diagram experimentally.

3.4. Hydrogen loading of fixed Pd–Au lattice: random and para-equilibrium

We are now ready to include Au in the MC simulations. To this end, we note that the two sublattices are markedly different from a kinetic perspective. Hydrogen diffuses easily even at low temperatures, while Pd and Au diffuse over a much longer timescale. To reach full equilibrium, in which the Pd and Au atoms rearrange in response to a change in hydrogen environment, a very slow experiment with H_2 pressure kept constant over extended periods of time, is required (see Sect. 4 below). If the H_2 pressure is more quickly increased/decreased, we may instead assume that the Pd–Au sublattice is frozen and that a metastable equilibrium is reached by rearrangement of the hydrogen atoms only. The chemical order on the Pd–Au sublattice would then typically be dictated by the conditions during fabrication of the alloy, which usually involve a form of thermal annealing. Here, we distinguish two extremes of such a metastable equilibrium: *para-equilibrium*, in which the Pd–Au ordering is equilibrated at 300 K in the absence of H_2, and *random equilibrium*, in which the Pd–Au lattice is randomized, corresponding to quenching of the system after equilibration at a very high temperature in absence of H_2.

We can model these situations by only carrying out VCSGC-MC flips on the H/vacancy sublattice. For the random equilibrium, we commence from a simulation cell in which the Pd and Au atoms have been randomly distributed, whereas for para-equilibrium, we run a canonical MC simulation with only Pd and Au and randomly pick a configuration as the fixed Pd–Au lattice. To suppress spurious effects from the particular choice of Pd–Au lattice, we averaged our results over five instances of both cases.

These MC simulations reveal weak short-range order (SRO) (Fig. 5, for definitions see Supplementary Note 5). We first note that the equilibration of the Pd–Au lattice in absence of hydrogen yields a weak propensity for the system to form unlike (Pd–Au) nearest neighbor bonds, whereas bonds that are alike (Au–Au and Pd–Pd) are weakly favored among next-nearest neighbors (Fig. 5a; in random Pd-Au the corresponding order parameters are zero by construction). For nearest neighbor Pd/Au–H/vacancy pairs (Fig. 5b–c), the SRO parameter is negative, indicating that H is more likely to occupy sites next to Pd than next to Au. This confirms what has been observed both with Mössbauer spectroscopy [53] and first-principles calculations [24], namely that it is energetically unfavorable for hydrogen to occupy the sites closest to a Au atom. For next-nearest Pd/Au–H/vacancy neighbors (Fig. 5d–e), on the other hand, the effect is reversed, albeit weaker. The change of sign between first and second nearest-neighbor was observed also by Sonwane *et al.* [54] in a model based on DFT calculations. It is furthermore consistent with the common argument that chemistry causes repulsion between neighboring Au and H, whereas dilation of the lattice by a Au atom gives rise to a more long-ranged elastic attraction [20].

The most pronounced difference between the two types of equilibria is found for the most short-ranged H/vacancy pair (Fig. 5f–g), for which the system in para-equilibrium has a stronger tendency to form H–H pairs. For next-nearest neighbor H/vacancy pairs (Fig. 5h–i) a more complex behavior emerges, with the sign of the SRO parameter being dependent on both H and Au concentration. For high H and Pd content, the SRO parameter is negative,

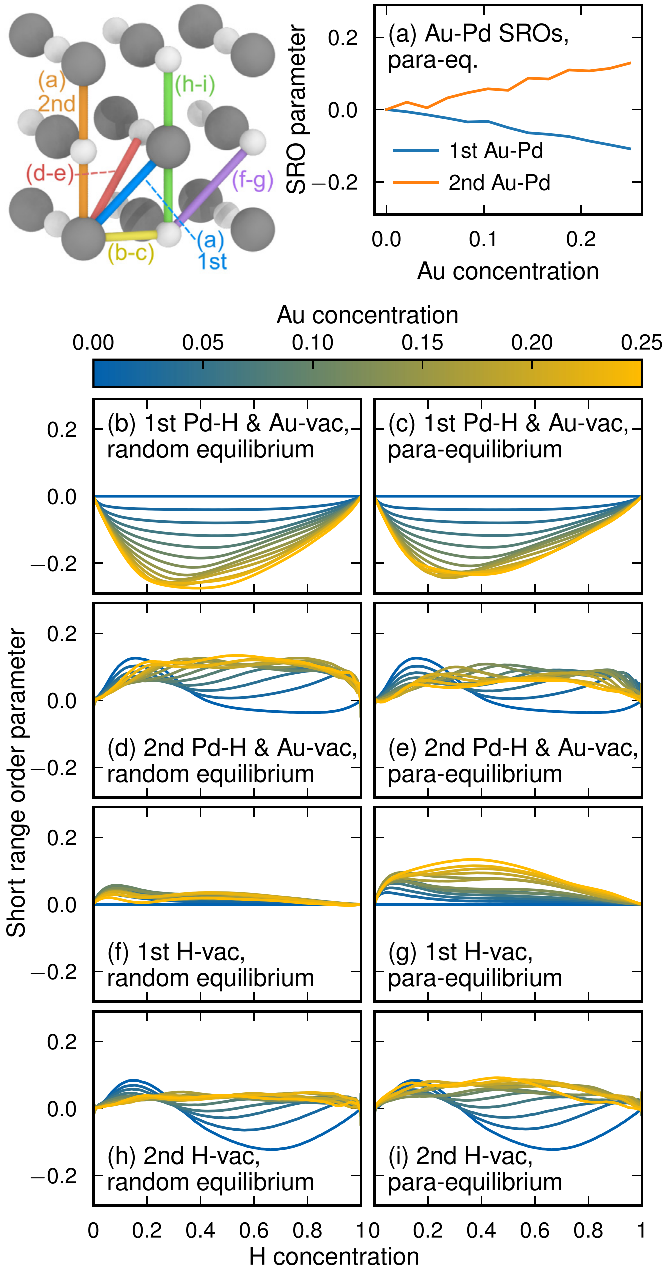

Fig. 5. SRO at 300 K in Pd–Au–H with the Pd–Au lattice fixed in a random configuration (left column) and as equilibrated in absence of H (para-equilibrium, right column). The SRO in the nearest-neighbor shell between the Pd/Au and the H/vacancy lattices (a–b) is negative, which, with our definitions (see Supplementary Note 5), means that H tends to sit close to Pd and vacancies close to Au. In the second Au/Pd shell (c–d), a weak reverse trend is seen throughout most of the H concentration range. In the first H/vacancy shell (f–g), H–H pairs are favored, only weakly in random equilibrium but stronger in para-equilibrium. The behavior is more complex in the second H/vacancy shell, with ordering tendencies being dependent on both H and Au concentrations.

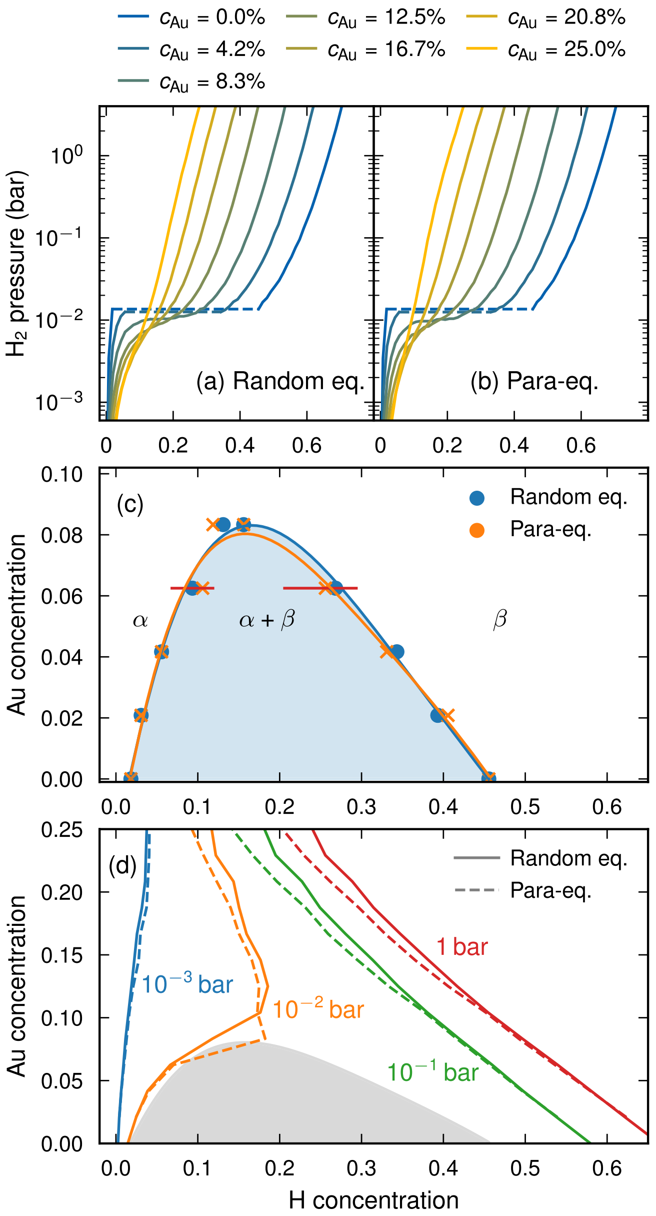

Fig. 6. Pressure–composition isotherms at 300 K for Pd–Au–H with (a) a random Pd–Au sublattice and (b) in para-equilibrium, i.e., with the Pd–Au lattice equilibrated at 300 K in absence of H. Phase transitions from the H-poor α phase to the H-rich β phase are indicated with a dashed line. The corresponding two phase diagrams (c) are almost identical, with the two-phase region closing at approximately 8-9% Au. Red lines at 6.3% Au indicate the range of values obtained from ten sampled CEs. By studying the hydrogen uptake at fixed H_2 pressure as a function of Au concentration (d), it is clear that differences between random and para-equilibrium are found primarily at high H_2 pressures, where at the same pressure the random system absorbs a slightly larger amount of hydrogen than the system in para-equilibrium. Larger variations are also seen at 10^{-2}bar (orange line), since this it close to the plateau pressure. The phase diagram in para-equilibrium is indicated with transparent grey in (d).

indicating that H atoms are distributed throughout the material, as H–H pairs are not favored. With a high content of Au and/or low content of H, the opposite behavior occurs, i.e., there is a slight excess of H–H pairs. This effect is somewhat more pronounced in para-equilibrium.

Given the quantitative difference in chemical ordering between random Au–Pd and para-equilibrium, we may now look for consequences for their respective thermodynamics. It turns out, however, that their H_2 pressure–composition isotherms (Fig. 6a–b) are very similar. It is only at fairly high Au concentrations, approaching 25% Au, that the isotherms of random and para-equilibrium exhibit discernible differences. At high Au concentrations and high H_2 pressures, the hydrogen uptake is slightly higher in random equilibrium than in para-equilibrium (Fig. 6d). Although this difference is small, there seems to be a weak but consistent trend; when SRO emerges due to lower annealing temperature, the hydrogen uptake at 300 K goes down at pressures above approximately 10mbar (Fig. S7). The difference seems to be the largest at a hydrogen pressure around 1bar, where the fully random alloy with 25% Au absorbs almost 4 percentage points more hydrogen than the one equilibrated in 300 K. These results seem to be in agreement with Chandrasekhar and Sholl [30]. To summarize, the SRO that emerges at low temperatures in Pd–Au makes the material absorb slightly less hydrogen at high H_2 pressures.

The discontinuity in the Au-poor isotherms, which is the hallmark of the phase transition from α to β, disappears quickly when the Au content is increased and it does so in almost exactly the same way for random and para-equilibrium. Consequently, the respective phase diagrams are essentially identical (Fig. 6c). Our results predict a critical Au concentration for the $\alpha + \beta$ two-phase region around 8–9%. This is significantly lower than experimental measurements, which yield estimates that vary from 10–15% (at 303 K) [11] to around 17% (at 298 K) [10]. The prediction of the *solvus* line is, however, sensitive to small variations in the ECIs (quantified by the spread obtained by sampling ten cluster expansion and indicated by red horizontal bars in Fig. 6c). Thus both our prediction and the experimental value are associated with significant uncertainties.

3.5. Hydrogen loading in full equilibrium

We may now ask what will happen if we allow the Pd–Au lattice to rearrange as we expose it to hydrogen. This situation is commonly referred to as full (or complete) equilibrium. It should be noted that this is an idealization that is very time-consuming to achieve in practice, as in most experiments the H_2 pressure is not maintained long enough to allow for Pd and Au to diffuse to a sufficient extent. Yet, it is important as it provides the thermodynamic driving force for the changes that do occur, although they may only rarely take the system to full equilibrium. To investigate the full equilibrium, we carried out MC simulations in the VCSGC ensemble on both sublattices. Subsequently we obtained the free energy by integration across the concentration plane using many different integration paths, and sampled the convex hull based on these different integration paths (for details, see Supplementary Note 6). Thereby we obtained a heat map of the probability that certain compositions are on the convex hull, which can be interpreted as (an isothermal cut of) the phase diagram (Fig. 7; see Fig. S10 for data at 250 and 500 K). The two-phase region at low Au content observed in para and random equilibrium is present in the full phase diagram at 300 K as well, but is accompanied by a much larger multi-phase region at higher Au concentrations (Fig. 7a). At 400 K, the former two-phase region is almost gone, but the multi-phase region at higher Au contents is still present. This new multi-phase region that appears in the full phase diagram, as opposed to random and para-equilibrium, is largely driven by a particularly stable composition interval around 25% Au and approximately 10–30% H, where at 300 K isobars ranging from 10^{-3}bar to 10^{2}bar all converge. A closer look at this composition interval reveals that LRO develops here (Fig. S9). Specifically, the Pd–Au sublattice orders in the $L1_2$ phase, in which the atoms are arranged such that 25% of the hydrogen sites are octahedral “cages” with only Pd nearest neighbors (Fig. 3b). As has been previously reported [24] and can be expected from the ECIs (Fig. 2), occupation of hydrogen at such sites is energetically particularly favorable, and renders this long-range ordered phase particularly stable. At 500 K (Fig. S10b), LRO no longer forms and the phase diagram is largely featureless, i.e., a solid solution can be expected at any concentration (except possibly at high Au content and extremely high H_2 pressures).

The phase diagram in Fig. 7a thus predicts that if a Pd–Au alloy at 300 K with, say, approximately 15% Au is subjected to a H_2 pressure between approximately 10^{-3}bar and 10^{2}bar, phase separation will occur. Of the resulting two phases, one will be the $L1_2$ phase with between 10 and 30% H. The character of the other phase depends on the H_2 pressure; if the pressure is below 10^{-2}bar, the second phase will be the dilute α phase (with Au content strongly dependent on H_2 pressure) whereas if the pressure is above approximately 10^{-2}bar, the second phase will be the hydrogen-rich β phase with approximately 5% Au.

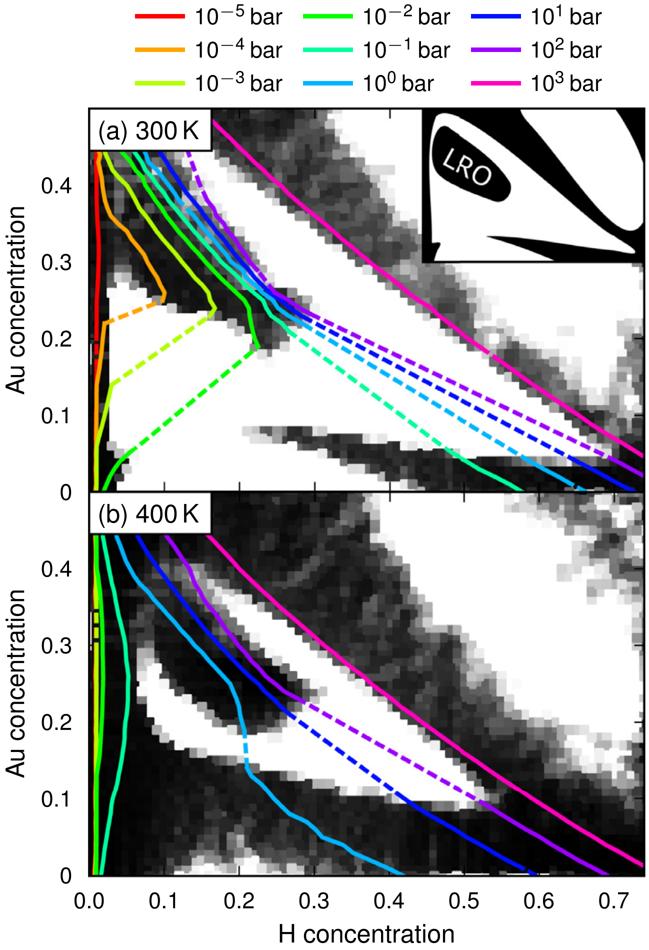

Fig. 7. Phase diagram of hydrogenated Pd–Au in full equilibrium at (a) 300 K and (b) 400 K. Black areas indicate single-phase regions, whereas white areas are multi-phase regions. Isobars (lines of fixed H_2 partial pressure) are drawn with colored lines. Many of the isobars converge in a region around 25% Au and 25% H, where the system exhibits LRO. The remaining dark areas represent a solid solution. The inset shows a schematic representation of the phase diagram to aid its interpretation.

The existence of a long-range ordered phase in hydrogen-treated Pd–Au has been reported experimentally by Lee *et al.* [29], who observed a super-lattice phase in Pd–Au with 19% Au. The structure of this phase could not be determined but the authors reported it to be more complex than $L1_2$. It should perhaps not be ruled out, however, that the off-stoichiometric composition as well as defects such as anti-phase boundaries, which occurred frequently in some of our simulations, may have played a role in these experiments. Importantly, these experiments provide us with an approximate time scale for the transformation between ordered and disordered phases. Specifically, “diagnostic” hydrogen-loading isotherms indicate that at 523 K changes in order take place gradually over many hours [29].

Another region of interest in Fig. 7 is the single-phase region that the 10^{3}bar isobar traces out (pink line in Fig. 7). Here, the SRO parameter for nearest neighbor Pd–Au pairs switches sign, indicating a transition from an excess of Pd–Au pairs to an excess of Au–Au and Pd–Pd pairs (Fig. S8). Inspection of the MC trajectories at these composition reveals that the system has started to cluster into hydrogen-poor Au clusters and hydrogen-rich Pd clusters, both only a few atoms large. Our model considers this phase thermodynamically stable and *not* merely a first step towards full phase separation. It seems plausible that a phase like this may provide a favorable balance between the short-ranged repulsion between Au and H and the long-ranged elastic attraction caused by dilation of the Pd lattice by adjacent Au clusters. It is not surprising that this phase has not been reported experimentally given the very high H_2 pressure required for it to form ($\gtrsim 10^3$bar). It should be noted that the pressure specified in this region is highly approximate, as this is outside the applicability range of the ideal gas law.

3.6. Impact of annealing conditions on hydrogen solubility

Although full equilibrium will usually not be reached in the time frame of a typical hydrogen loading experiment, there may be circumstances in which full equilibrium is approached. For example, annealing of Pd–Au is sometimes done in the presence of hydrogen in order to prevent oxidation. Although the pressure of H_2 is then typically too low to have a significant impact, the phase diagram Fig. 7 shows that complex behavior may emerge in the presence of hydrogen, especially if the temperature is not too high. We may consider a fairly typical situation in which the alloy is annealed at a particular temperature and H_2 pressure, after which hydrogen absorption/desorption isotherms are measured at another temperature. Since the latter absorption/desorption is usually carried out at a much lower temperature than the annealing, and during a much shorter period of time, it is reasonable to assume that the Pd–Au sublattice gets frozen in during annealing and does not change when measuring the isotherm. The chemical ordering on the Pd–Au sublattice would then be determined entirely by the conditions during annealing.

We now mimic such an experiment by simulating isotherms at 300 K in Pd–Au with 25% of Au annealed in different conditions. To this end, we first run MC simulations at a specified annealing temperature with canonical MC swaps on the Pd–Au sublattice, and SGC MC flips on the H–vacancy sublattice, using a chemical potential corresponding to a fixed H_2 pressure. We then pick five random snapshots from the resulting trajectory, remove the hydrogen, fix the Pd–Au sublattice, and run MC simulations at 300 K with SGC flips on the H–vacancy sublattice only, using a wide range of hydrogen chemical potentials.

Inspection of 300 K isotherms with Pd–Au annealed in 400 K (Fig. 8a) reveals that the hydrogen concentration depends strongly on the conditions during annealing. When annealed in pressures of 10^{-1}bar or lower (blue and orange lines), the isotherms behave as in the random or para-equilibrium case, with an almost linear isotherm (when plotted on a logarithmic scale). For higher pressures, however, the isotherms are markedly different. After annealing in 1, 10 or 100bar, the uptake of hydrogen at low pressures is much higher, after which the concentration of hydrogen stays at about 25% up to very high pressures, meaning that at sufficiently high pressures, the hydrogen content is in fact higher in Pd–Au samples that were annealed in the absence of hydrogen. The difference between these two kinds of isotherms is that annealing in 1–100bar induces $L1_2$ LRO. If the H_2 pressure is raised to 1,000bar, the ordered phase no longer forms, and the isotherm (brown line in Fig. 8a) becomes more similar to the low-pressure isotherms, although the hydrogen uptake is significantly higher if the H_2 pressure is above a few millibar.

The ordered $L1_2$ phase is thus clearly distinguishable from the ones lacking LRO already from the isotherms. These findings are consistent with Lee *et al.* [29]. When annealing in 600 K, on the other hand, the temperature is too high for any LRO to emerge, and the 600 K isotherms are essentially identical regardless of annealing pressure (Fig. 8b). It is expected that much higher pressures are required to impact the system at 600 K compared to 400 K, because at constant pressure when the temperature goes up, the hydrogen content in the material goes down. Nevertheless, when the annealing pressure is 100bar, the hydrogen content in the system is about 14% during annealing, but the 300 K isotherm is still virtually unaffected. Only when the annealing pressure reaches 1,000bar (leading to approximately 26% hydrogen in the system during annealing), is the isotherm clearly distinguishable from the isotherm of Pd–Au annealed in vacuum, and even then the difference is small.

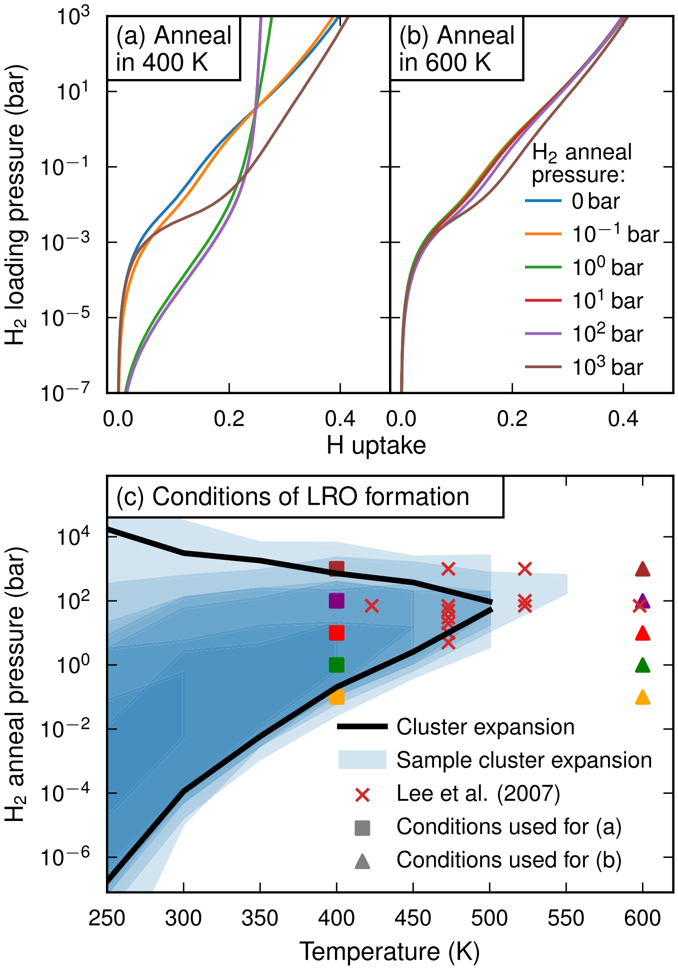

Fig. 8. Impact of annealing conditions on absorption of H in Pd–Au with 25% Au at 300 K. After annealing in 400 K (a), the isotherms exhibit a markedly different behavior if the H_2 pressure during annealing was between 1 and 100bar (the red 10bar isotherm is hidden under the green 1bar isotherm). After annealing in 600 K (b), the isotherms are almost identical regardless of H_2 exposure during annealing. The origin of the change in isotherm in (a) is the formation of LRO under certain conditions as quantified in (c). The CE predicts that LRO will form in full equilibrium when Pd–Au with 25% Au is subjected to H_2 pressure and temperature corresponding to the area between the black lines. The corresponding area predicted with ten sampled CEs is indicated with transparent blue, one per CE. Darker color thus means more cluster expansion predict order formation at that point. Out of these ten cluster expansion, two have a critical temperature too low to be visible in this figure. The conditions investigated by Lee *et al.* [29] with signs of order formation in Pd–Au with 19% Au are indicated with red crosses. Colored squares and triangles indicate the annealing conditions for isotherms in (a) and (b), respectively.

This picture emerges more comprehensively if we study the hydrogen absorbed at 300 K and specific partial pressures (Fig. S11): the content of hydrogen is virtually independent of annealing conditions as long as the phase transition to the $L1_2$ phase does not occur. Very high annealing pressures, on the order of 10–1000bar, are required to achieve a significant impact on the content of absorbed hydrogen unless the ordered $L1_2$ phase is formed.

It is worth stressing that while hydrogen uptake at moderate pressure is enhanced by LRO formation, we observe a different trend in Sect. 3.4; SRO formation decreases the hydrogen uptake unless the pressure is very low. It is thus advisable not to speak in too general terms about the impact of chemical order on hydrogen solubility, because it depends on the details of the chemical order as well as the H_2 pressure at which the solubility is assessed.

Given that the chemical ordering of the $L1_2$ phase thus has a significant impact on the nature of absorption of H_2 in Pd–Au, it may have a notable impact on any utilization thereof. We therefore estimate the conditions during which this long-range ordered phase will form (Fig. 8c). Our CE indicates that the ordered structure starts to form below approximately 500 K with a H_2 pressure between approximately 50 and 100bar. The H_2 pressure range where LRO forms then widens quickly as temperature is decreased, but slower kinetics will of course inhibit order formation at too low temperatures. Lee *et al.* [29], who studied Pd–Au with 19% Au, assumed that distinct isotherms are a fingerprint of LRO, and while the purpose of their study was not to map out the conditions under which order emerges, their observations are qualitatively consistent with our CE (red crosses in Fig. 8c), but with a higher critical temperature (with LRO persisting up to at least 598 K). It thus seems likely that our CE underestimates the critical temperature by at least 100 K. By repeating the same calculations with 10 different cluster expansion (blue areas in Fig. 8c), we observe qualitatively the same behavior but find that both the critical temperature and the pressure range are very sensitive to small variations in the ECIs. Although none of the sampled cluster expansion exhibit a critical temperature above 600 K, it should be clear that small errors not captured by the CE approach (such as neglect of vibrations or the choice of exchange-correlation functional used to calculate the training data) may cause an error of this magnitude.

4. Conclusions

We have comprehensively investigated the impact of chemical order on hydrogenation of Pd–Au alloys using a computational approach based on DFT calculations, CE models, and MC simulations. Although relatively large relaxations from octahedral hydrogen sites hamper the ability of the CE models to exactly reproduce formation energies calculated with DFT, we found that our CE reproduced thermodynamic properties of Pd–Au–H that are well-established experimentally, with a quantitative agreement on par with what can be expected from a CE approach. This applies especially given the large impact of small changes in the ECIs, which is likely always inherent in this approach or indeed any other approach for deriving phase diagrams from interatomic potentials or first-principles data. Vibrational contributions, including the zero-point energy, can sometimes play an important role in hydrides due to the low mass of hydrogen, but inclusion of these effects would have been computationally prohibitive. Moreover, we note that tetrahedral hydrogen sites can play a role, although they are usually energetically much less favorable than octahedral sites [24,42]. These effects may contribute to some of the quantitative disagreement with experiment since especially vibrations have been shown to have a notable impact on phase diagrams [55–57].

Our results provide a rationale for the experimental observation that absorption/desorption isotherms are relatively stable over time; as long as the $L1_2$ phase does not form, isotherms will stay similar even if chemical order changes. This is manifested by the similarity between isotherms in random and para-equilibrium. Our results predict that a small reduction in the ability to absorb hydrogen may be observed if Pd–Au annealed at a very high temperature is allowed to reach equilibrium at a much lower temperature. We emphasize that the present results are strictly valid only for the bulk material, and do not take into account potentially important effects such as agglomeration of hydrogen in grain boundaries, surface fouling or surface segregation, which should be kept in mind when comparing with experiment.

Under long-term exposure to hydrogen, however, the situation changes substantially. The emergence of the ordered $L1_2$ phase introduces complexity in the phase diagram, and Pd–Au stored at room temperature and, say, 1mbar H_2 may over time exhibit very different absorption isotherms, as the result of emerging LRO. The hydrogen content in air is of course orders of magnitude lower than what we predict is required for this phase to form, but repeated exposure to high H_2 pressures may result in formation of LRO and an altered isotherm. Such conditions are found for example in membrane reactors for hydrogen gas production [58]. While we did not address kinetic aspects in this study, earlier experiments provide an approximate time scale for the transformation, as samples annealed at 523 K were observed to exhibit a gradual transition over many hours [29].

Does the LRO vanish when the hydrogen is removed? This question is difficult to answer, because our simulation approach is not able to describe the kinetic stability of the ordered phase in absence of hydrogen (or vice versa). We do predict that the $L1_2$ phase is the ground state at this composition also in absence of hydrogen, but its critical temperature is well below 300 K. It may, however, be noted that there are (hydrogen-free) Pd–Au phase diagrams in the literature where this phase is expected to form above room temperature [47,48,51], that is, even without exposure to hydrogen. Although the existence of this phase, let alone its critical temperature, remains debated, it seems reasonable to assume that the $L1_2$ phase might be fairly stable at room temperature even after hydrogen is removed. One should note that time-dependent annealing experiments suggest that order→disorder and disorder→order transitions proceed on similar time scales [29]. In combination with the exponential temperature dependence of the diffusivity, one can thus expect the time-temperature history of, e.g., a membrane reactor, to play a crucial role.

The emergence of a different isotherm upon ordering might constitute a challenge as the sensor would have a different readout at the same H_2 pressure. It may, however, also present an opportunity. The ordered phase absorbs significantly more hydrogen at low pressures. A sensor consisting of the ordered phase is thus likely (depending on the nature of the readout) to be significantly more sensitive to small changes in H_2 pressure. If the phase is sufficiently stable, this may provide a relatively simple way to improve a Pd–Au hydrogen sensor—annealing in hydrogen to boost sensitivity.

Declaration of Competing Interest

The authors declare that they have no known competing financial interests or personal relationships that could have appeared to influence the work reported in this paper.

Acknowlgedgments

This work was funded by the Knut and Alice Wallenberg Foundation (grant numbers 2014.0226, 2015.0055), the Swedish Research Council (grant numbers 2018-06482, 2020-04935), and the Swedish Foundation for Strategic Research (grant number RMA15-0052). The computations were enabled by resources provided by the Swedish National Infrastructure for Computing (SNIC) at NSC, C3SE and PDC partially funded by the Swedish Research Council (grant number 2018-05973). We thank Dr. Jonatan Wårdh for helpful discussions.

Supplementary material

Supplementary material associated with this article can be found, in the online version, at 10.1016/j.actamat.2021.116893

References

[1] A. Schneemann, J.L. White, S. Kang, S. Jeong, L.F. Wan, E.S. Cho, T.W. Heo, D. Prendergast, J.J. Urban, B.C. Wood, M.D. Allendorf, V. Stavila, Nanostructured metal hydrides for hydrogen storage, Chemical Reviews 118 (22) (2018) 10775–10839, doi:10.1021/acs.chemrev.8b00313.

[2] C. Wadell, S. Syrenova, C. Langhammer, Plasmonic hydrogen sensing with nanostructured metal hydrides, ACS Nano 8 (12) (2014) 11925–11940, doi:10.1021/nn505804f.

[3] I. Darmadi, F.A.A. Nugroho, C. Langhammer, High-Performance Nanostructured Palladium-Based Hydrogen Sensors–Current Limitations and Strategies for Their Mitigation, ACS Sensors 5 (11) (2020) 3306–3327, doi:10.1021/acssensors.0c02019.

[4] T.C. Narayan, F. Hayee, A. Baldi, A.L. Koh, R. Sinclair, J.A. Dionne, Direct visualization of hydrogen absorption dynamics in individual palladium nanoparticles, Nature Communications 8 (1) (2017) 1–8, doi:10.1038/ncomms14020.

[5] F.A. Nugroho, I. Darmadi, L. Cusinato, A. Susarrey-Arce, H. Schreuders, L.J. Bannenberg, A.B. da Silva Fanta, S. Kadkhodazadeh, J.B. Wagner, T.J. Antosiewicz, et al., Metal–polymer hybrid nanomaterials for plasmonic ultrafast hydrogen detection, Nature Materials 18 (5) (2019) 489–495, doi:10.1038/s41563-019-0325-4.

[6] I. Darmadi, A. Stolaś, I. Östergren, B. Berke, F.A.A. Nugroho, M. Minelli, S. Lerch, I. Tanyeli, A. Lund, O. Andersson, V.P. Zhdanov, M. Liebi, K. Moth-Poulsen, C. Müller, C. Langhammer, Bulk-processed pd nanocube-poly(methyl methacrylate) nanocomposites as plasmonic plastics for hydrogen sensing, ACS Applied Nano Materials 3 (8) (2020) 8438–8445, doi:10.1021/acsanm.0c01907.

[7] T.B. Flanagan, W.A. Oates, The palladium-hydrogen system, Annual Review of Materials Science 21 (1) (1991) 269–304, doi:10.1146/annurev.ms.21.080191.001413.

[8] R. Griessen, N. Strohfeldt, H. Giessen, Thermodynamics of the hybrid interaction of hydrogen with palladium nanoparticles, Nature Materials 15 (3) (2016) 311–317, doi:10.1038/nmat4480.

[9] S. Syrenova, C. Wadell, F.A. Nugroho, T.A. Gschneidtner, Y.A.D. Fernandez, G. Nalin, D. Świtlik, F. Westerlund, T.J. Antosiewicz, V.P. Zhdanov, et al., Hydride formation thermodynamics and hysteresis in individual Pd nanocrystals with different size and shape, Nature Materials 14 (12) (2015) 1236–1244, doi:10.1038/nmat4409.

[10] A. Maeland, T.B. Flanagan, X-ray and thermodynamic studies of the absorption of hydrogen by gold-palladium alloys, The Journal of Physical Chemistry 69 (10) (1965) 3575–3581, doi:10.1021/j100894a054.

[11] S. Luo, D. Wang, T.B. Flanagan, Thermodynamics of hydrogen in fcc Pd-Au alloys, The Journal of Physical Chemistry B 114 (18) (2010) 6117–6125, doi:10.1021/jp100858r.

[12] C. Wadell, F.A.A. Nugroho, E. Lidström, B. Iandolo, J.B. Wagner, C. Langhammer, Hysteresis-Free Nanoplasmonic Pd–Au Alloy Hydrogen Sensors, Nano Letters 15 (5) (2015) 3563–3570, doi:10.1021/acs.nanolett.5b01053.

[13] F.A.A. Nugroho, I. Darmadi, V.P. Zhdanov, C. Langhammer, Universal scaling and design rules of hydrogen-induced optical properties in Pd and Pd-alloy nanoparticles, ACS Nano 12 (10) (2018) 9903–9912, doi:10.1021/acsnano.8b02835.

[14] R.J. Westerwaal, J.S.A. Rooijmans, L. Leclercq, D.G. Gheorghe, T. Radeva, L. Mooij, T. Mak, L. Polak, M. Slaman, B. Dam, T. Rasing, Nanostructured Pd-Au based fiber optic sensors for probing hydrogen concentrations in gas mixtures, International Journal of Hydrogen Energy 38 (10) (2013) 4201–4212, doi:10.1016/j.ijhydene.2012.12.146.

[15] L.J. Bannenberg, F.A.A. Nugroho, H. Schreuders, B. Norder, T.T. Trinh, N.-J. Steinke, A.A. van Well, C. Langhammer, B. Dam, Direct comparison of pdau alloy thin films and nanoparticles upon hydrogen exposure, ACS Applied Materials & Interfaces 11 (17) (2019) 15489–15497, doi:10.1021/acsami.8b22455.

[16] Y. Pak, Y. Jeong, N. Alaal, H. Kim, J. Chae, J.-W. Min, A.A.S. Devi, S. Mitra, D.H. Lee, Y. Kumaresan, W. Park, T.-W. Kim, I.S. Roqan, G.-Y. Jung, Highly stable and ultrafast hydrogen gas sensor based on 15 nm nanogaps switching in a palladium-gold nanoribbons array, Advanced Materials Interfaces 6 (4) (2019) 1801442, doi:10.1002/admi.201801442.

[17] A.J. Berry, LVI.–The occlusion of hydrogen by the palladium-gold alloys, Journal of the Chemical Society, Transactions 99 (1911) 463–466, doi:10.1039/CT9119900463.

[18] J. Schniedermann, Lichtelektrischer und thermoelektrischer Effekt wasserstoffbeladener Palladium-Silber und Palladium-Goldlegierungen, Annalen der Physik 405 (7) (1932) 761–779, doi:10.1002/andp.19324050702.

[19] Y. Sakamoto, F.L. Chen, M. Ura, T.B. Flanagan, Thermodynamic properties for solution of hydrogen in palladium-based binary alloys, Berichte der Bunsengesellschaft für physikalische Chemie 99 (6) (1995) 807–820, doi:10.1002/bbpc.19950990605.

[20] Y. Fukai, The metal-hydrogen system: basic bulk properties, 21, Springer Science & Business Media, 2006.

[21] A. Pundt, R. Kirchheim, Hydrogen in metals: Microstructural aspects, Annual Review of Materials Research 36 (1) (2006) 555–608, doi:10.1146/annurev.matsci.36.090804.094451.

[22] W. Huang, S.M. Opalka, D. Wang, T.B. Flanagan, Thermodynamic modelling of the Cu-Pd-H system, Calphad 31 (3) (2007) 315–329, doi:10.1016/j.calphad.2007.02.002.

[23] J.-M. Joubert, S. Thiébaut, A thermodynamic description of the system Pd-Rh-H-D-T, Acta Materialia 59 (4) (2011) 1680–1691, doi:10.1016/j.actamat.2010.11.035.

[24] M. Mamatkulov, V.P. Zhdanov, Suppression of hysteresis in absorption of hydrogen by a Pd–Au alloy, Phys. Rev. E 101 (2020) 042130, doi:10.1103/PhysRevE.101.042130.

[25] A. Hultgren, Isothermal transformation of austenite, Transactions of the American Society for Metals 39 (1947) 915–1005.

[26] M. Hillert, J. Ågren, On the definitions of paraequilibrium and orthoequilibrium, Scripta Materialia 50 (5) (2004) 697–699, doi:10.1016/j.scriptamat.2003.11.020.

[27] T.B. Flanagan, W. Oates, Para-equilibrium Phase Diagrams, $\mu_H - X_M$, for Pd Alloy-H Systems, Journal of Phase Equilibria and Diffusion 40 (2) (2019) 285–290, doi:10.1007/s11669-019-00724-0.

[28] D.E. Nanu, Y. Deng, A.J. Böttger, Unified approach for cluster variation method calculations of phase diagrams in fcc substitutional alloys with interstitial species, Physical Review B 74 (2006) 014113, doi:10.1103/PhysRevB.74.014113.

[29] S.-M. Lee, H. Noh, T.B. Flanagan, S. Luo, Hydrogen-induced lattice rearrangement of a $Pd_{0.81}Au_{0.19}$ alloy, Journal of Physics: Condensed Matter 19 (32) (2007) 326222, doi:10.1088/0953-8984/19/32/326222.

[30] N. Chandrasekhar, D.S. Sholl, Computational study of hydrogen induced lattice rearrangement and its influence on hydrogen permeance in Pd–Au alloys, Journal of Alloys and Compounds 609 (2014) 244–252, doi:10.1016/j.jallcom.2014.04.156.

[31] L. Semidey-Flecha, D.S. Sholl, Combining density functional theory and cluster expansion methods to predict H_2 permeance through Pd-based binary alloy membranes, The Journal of Chemical Physics 128 (14) (2008) 144701, doi:10.1063/1.2900558.

[32] N. Bourgeois, P. Cenedese, J.-C. Crivello, J.-M. Joubert, Pd–H and Ni–H phase diagrams using cluster variation method and Monte Carlo simulation, Philosophical Magazine 99 (19) (2019) 2376–2392, doi:10.1080/14786435.2019.1628367.

[33] N.S.H. Gunda, A. Van der Ven, First-principles insights on phase stability of titanium interstitial alloys, Physical Review Materials 2 (2018) 083602, doi:10.1103/PhysRevMaterials.2.083602.

[34] B. Ouyang, T. Chakraborty, N. Kim, N.H. Perry, T. Mueller, N.R. Aluru, E. Ertekin, Cluster Expansion Framework for the $Sr(Ti_{1-x}Fe_x)O_{3-x/2}$ $(0 < x < 1)$ Mixed Ionic Electronic Conductor: Properties Based on Realistic Configurations, Chemistry of Materials 31 (9) (2019) 3144–3153, doi:10.1021/acs.chemmater.8b04285.

[35] G.L.W. Hart, R.W. Forcade, Algorithm for generating derivative structures, Physical Review B 77 (2008) 224115, doi:10.1103/PhysRevB.77.224115.

[36] M. Ångqvist, W.A. Muñoz, J.M. Rahm, E. Fransson, C. Durniak, P. Rozyczko, T.H. Rod, P. Erhart, Icet – a python library for constructing and sampling alloy cluster expansions, Advanced Theory and Simulations 2 (7) (2019) 1900015, doi:10.1002/adts.201900015.

[37] G. Kresse, J. Furthmüller, Efficiency of ab-initio total energy calculations for metals and semiconductors using a plane-wave basis set, Computational Materials Science 6 (1) (1996) 15–50, doi:10.1016/0927-0256(96)00008-0.

[38] G. Kresse, D. Joubert, From ultrasoft pseudopotentials to the projector augmented-wave method, Physical Review B 59 (1999) 1758–1775, doi:10.1103/PhysRevB.59.1758.

[39] M. Dion, H. Rydberg, E. Schröder, D.C. Langreth, B.I. Lundqvist, Van der waals density functional for general geometries, Phys. Rev. Lett. 92 (2004) 246401, doi:10.1103/PhysRevLett.92.246401.

[40] K. Berland, P. Hyldgaard, Exchange functional that tests the robustness of the plasmon description of the van der Waals density functional, Physical Review B 89 (2014) 035412, doi:10.1103/PhysRevB.89.035412.

[41] J. Sanchez, F. Ducastelle, D. Gratias, Generalized cluster description of multicomponent systems, Physica A: Statistical Mechanics and its Applications 128 (1) (1984) 334–350, doi:10.1016/0378-4371(84)90096-7.

[42] D. Nanu, W. Legerstee, S. Eijt, W. Haije, J. Vente, M. Tucker, A. Böttger, Insights into the relation between crystal structure and deuterium desorption characteristics of Pd–Au–D alloys, Acta Materialia 56 (20) (2008) 6132–6140, doi:10.1016/j.actamat.2008.08.045.

[43] T. Mueller, G. Ceder, Bayesian approach to cluster expansions, Physical Review B 80 (2009) 024103, doi:10.1103/PhysRevB.80.024103.

[44] D. Foreman-Mackey, D.W. Hogg, D. Lang, J. Goodman, emcee: The MCMC hammer, Publications of the Astronomical Society of the Pacific 125 (925) (2013) 306–312, doi:10.1086/670067.

[45] B. Sadigh, P. Erhart, Calculation of excess free energies of precipitates via direct thermodynamic integration across phase boundaries, Physical Review B 86 (2012) 134204, doi:10.1103/PhysRevB.86.134204.

[46] B. Sadigh, P. Erhart, A. Stukowski, A. Caro, E. Martinez, L. Zepeda-Ruiz, Scalable parallel monte carlo algorithm for atomistic simulations of precipitation in alloys, Physical Review B 85 (2012) 184203, doi:10.1103/PhysRevB.85.184203.

[47] Y. Matsuo, A. Nagasawa, J. Kakinoki, Ordered Alloys of the Gold-Palladium System. II. Electron Diffraction Study on Evaporated $AuPd_3$ Films, Journal of the Physical Society of Japan 21 (12) (1966) 2633–2637, doi:10.1143/JPSJ.21.2633.

[48] Y. Kawasaki, S. Ino, S. Ogawa, Electron diffraction study on the superlattice formation in the gold-palladium alloy system, Journal of the Physical Society of Japan 30 (6) (1971) 1758–1759, doi:10.1143/JPSJ.30.1758.

[49] J. Nelayah, N.T. Nguyen, D. Alloyeau, G.Y. Wang, C. Ricolleau, Long-range chemical orders in Au–Pd nanoparticles revealed by aberration-corrected electron microscopy, Nanoscale 6 (2014) 10423–10430, doi:10.1039/C4NR01427H.

[50] S.V. Barabash, V. Blum, S. Müller, A. Zunger, Prediction of unusual stable ordered structures of Au-Pd alloys via a first-principles cluster expansion, Physical Review B 74 (2006) 035108, doi:10.1103/PhysRevB.74.035108.

[51] F. Berthier, B. Legrand, Analysis of Au–Pd driving forces via the effective site energy model: LRO, antisites and enthalpy of permutation, Journal of Physics: Condensed Matter 32 (35) (2020) 354001, doi:10.1088/1361-648x/ab87ce.

[52] E. Wicke, J. Blaurock, New experiments on and interpretations of hysteresis effects of Pd-D_2 and Pd-H_2, Journal of the Less Common Metals 130 (1987) 351–363, doi:10.1016/0022-5088(87)90129-9.

[53] F.E. Wagner, M. Karger, F. Pröbst, B. Schüttler, Interaction of Hydrogen with Substitutional Solute Metals in the ß-Phase of the Palladium-Hydrogen System, Springer US, Boston, MA, pp. 581–588. 10.1007/978-1-4684-7630-9_82

[54] C.G. Sonwane, J. Wilcox, Y.H. Ma, Solubility of hydrogen in PdAg and PdAu binary alloys using density functional theory, The Journal of Physical Chemistry B 110 (48) (2006) 24549–24558, doi:10.1021/jp064507t.

[55] A. van de Walle, G. Ceder, The effect of lattice vibrations on substitutional alloy thermodynamics, Reviews of Modern Physics 74 (2002) 11–45, doi:10.1103/RevModPhys.74.11.

[56] A. Böttger, D. Nanu, A. Marashdeh, The γ-Fe[N] and γ'-Fe_4N_{1-x} phase boundaries in high-nitrogen steels: The cube cluster approximation and the effect of vibrational energy contributions, Computational Materials Science 95 (2014) 8–12, doi:10.1016/j.commatsci.2014.07.004.

[57] M. Gren, E. Fransson, M. Ångqvist, P. Erhart, G. Wahnström, Modeling of vibrational and configurational degrees of freedom in hexagonal and cubic tungsten carbide at high temperatures, Physical Review Materials 5 (3) (2021) 033804, doi:10.1103/PhysRevMaterials.5.033804.

[58] G. Bernardo, T. Araújo, T. da Silva Lopes, J. Sousa, A. Mendes, Recent advances in membrane technologies for Hydrogen purification, International Journal of Hydrogen Energy 45 (12) (2020) 7313–7338 Hydrogen separation/purification via membrane technology., doi:10.1016/j.ijhydene.2019.06.162. Hydrogen separation/purification via membrane technology